Plasma enhanced anti-coking performance of Pd/CeO_2 catalysts for conversion of methane

Received 00th January 20xx,
Accepted 00th January 20xx

DOI: 10.1039/x0xx00000x

Xiucui Hu,[a] Yadi Liu,[a] Liguang Dou,[a] Cheng Zhang,[a, b] Shuai Zhang,[a, b] Yuan Gao,[a] Xin Tu[c] and Tao Shao[a, b *]

The direct nonoxidative conversion of methane (CH_4) to valuable chemicals has attracted increasing interests. However, the carbon deposition will inevitably occur due to CH_4 decomposition at high temperature. Here, we report the conversion of CH_4 assisted by the non-thermal plasma into olefins and H_2 over a Pd/CeO_2 catalyst. The addition of the plasma could effectively enhance the anti-coking performance of the catalyst, facilitating conversion the CH_4. The interaction between plasma and catalyst was explored in detail. The energized electron and ions generated by plasma could impact with adsorbed CH_3 species to efficiently suppress the consequent dehydrogenation of the adsorbed CH_3, accelerating CH_3 species to desorb from the surface of the catalyst, thus reduced the amount of the carbon deposition on catalyst surface. The highly efficient catalysts assisted by plasma is effective to enhance the CH_4 conversion and suppress the carbon deposition, which deserved to be widely application in catalysis.

1. Introduction

The continuous fossil energy consumption and the increasingly emerging environmental problems have made alternative renewable and sustainable energy resources attract widespread attention.[1] Particularly, CH_4 as a primary component of natural gas is considered as one of the alternatives to nonrenewable coal and crude oil due to its huge reserves and its upgrading to valuable hydrocarbon feedstocks (such as aromatics, olefins, oxygenates) and hydrogen.[2-4] However, excessive cracking of CH_4 can lead to carbon deposition and catalyst deactivation, thus the strategies to minimize excessive cracking of CH_4 are important in CH_4-containing reaction such as the conversion of CH_4 and biogas reforming technology (CH_4/CO_2 conversion).[5]

The CH_4 conversion can be conventionally achieved either by indirect methods concerning multiple catalytic transformations such as through synthesis gas (a mixture of CO and H_2)[6, 7] and methanol[8] or by direct methods consisting of oxidative coupling of methane (OCM),[9, 10] nonoxidative dehydroaromatization of methane (MDA)[11, 12] and nonoxidative conversion of methane to olefins, aromatics, and hydrogen (MTOAH).[13-15] Among them, the MTOAH route is a promising approach for CH_4 conversion to C_2 products (C_2H_4 and C_2H_2) and hydrogen due to zero emissions of carbon dioxide and maximum carbon atom utilization.[13, 14] However, it still remains a grand challenge to achieve the CH_4 activation at low temperature because of the highest C-H bond strength (434 kJ mol^{-1}), the high ionization energy, the low electron affinity and polarizability.[16, 17]

It has been reported that single Fe atoms embedded in SiO_2 matrix (Fe©SiO_2) at 950−1,090 °C possessed high catalytic selectivity for the nonoxidative conversion of CH_4 to ethylene (C_2H_4), aromatics (benzene, naphthalene) and H_2.[13] The conversion of CH_4 reached 48.1% and the selectivity of ethylene exceeded 48% at 1,090 °C. The C-H of CH_4 was activated over atomic Fe sites to form methyl (CH_3) radicals. The CH_3 radicals diffused easily from the catalyst surface into the gas phase to trigger chain reaction ($CH_3 + CH_3 \rightarrow C_2H_6$), which subsequently underwent a series of gas-phase reactions to generate the target products. No coke deposition was observed because the absence of Fe ensembles suppressed C-C coupling and carbon coking under the high-temperature catalytic conditions.[13] The development of the stable single-atom catalyst at high temperature during CH_4 conversion reaction provides a new route to inhibit carbon deposition. Dipu A. *et al* has reported that the CH_4 was activated over the Ni-P/SiO_2 catalysts,[15] which showed the high selectivity (99.9%) of ethane and ethylene at 850 °C with the low selectivity (0.1%) of carbon (C) deposition, although the conversion of methane was only 0.08%. The activation of CH_4 firstly generated ethane (C_2H_6) via two CH_3 radicals coupled each other as the primary product on the catalyst surface, and then the thermal conversion of C_2H_6 to other target products (olefins and benzene) in the gas phase.[15] The above results showed for the CH_4 conversion, it is crucial to suppress the carbon deposition through tuning the generation and desorption of CH_3 species over catalysts and guiding the subsequent a series of reactions in the gas phase. However, the active metal species not only aggregate inevitably into larger nanoparticles but also are easy inactivated at high temperatures (ca. 1,000 °C). Therefore, an innovative technique for the direct conversion of CH_4 process is highly desirable.

The low-temperature activation of CH_4 with highly reactive catalysts assisted by non-thermal plasma (NTP) is a promising strategy to achieve the CH_4 conversion more efficient and selective, because NTP can generate extremely active electrons with a mean electron energy of 1–10 eV,[18-20] which can activate inert molecules (e.g., CH_4 or CO_2) at atmospheric pressure and low temperatures into reactive species, such as excited atoms, molecules, ions and radicals (CH_3 radicals and H radicals).[21, 22] Until now, much efforts have concentrated on direct nonoxidative conversion of methane using various NTPs with or without a catalyst, including dielectric barrier discharge (DBD),[23, 24] pulsed discharge,[25, 26] spark discharge,[27] radio-frequency discharge,[28] corona discharge[29] and microwave discharge.[30] Particularly, the nanosecond pulsed discharge (NPD) has attracted much attention because of its unique features, such as higher energy efficiency,[31] the extreme non-equilibrium character,[32] massive high energy electrons,[33] the short pulse duration suppressing the transition from plasma to thermal-equilibrium

[a] Beijing International S&T Cooperation Base for Plasma Science and Energy Conversion, Institute of Electrical Engineering, Chinese Academy of Sciences, Beijing 100190, China. E-mail: st@mail.iee.ac.cn
[b] University of Chinese Academy of Sciences, Beijing 100049, China.
[c] Department of Electrical Engineering and Electronics, University of Liverpool, Liverpool L69 3GJ, United Kingdom.

† Electronic Supplementary Information (ESI) available: [details of any supplementary information available should be included here]. See DOI: 10.1039/x0xx00000x

state.[34] However, the high conversion of CH_4 and selectivity of the olefins still remains a grand challenge. Thus, combining both advantages of catalyst and plasma was a promising route.

For the efficient catalyst materials, ceria (CeO_2) as a well-known functional rare earth material has been extensively used as catalyst support in a variety of catalytic reactions owing to its unique oxygen storage and release capacity.[35] In addition, ceria can greatly overcome the sintering of the deposited metal to disperse and stabilize the metals as small-size species, even ultra-fine clusters or single atoms at high temperature by tuning the interaction between the active metal and CeO_2 support.[36, 37] Ceria-supported Pd catalysts have shown some promising properties for CH_4 activation,[35, 38] while the formation of carbon deposition is disadvantaged for its catalytic applications.

Herein, we reported Pd/CeO_2 with low loading for the direct nonoxidative conversion of CH_4 into light hydrocarbons and H_2 assisted by nanosecond pulsed DBD at atmospheric pressure to reduce the amount of carbon deposition. A notable enhancement on the CH_4 conversion for the plasma-catalysis compared with the catalysis-only. The introduction of plasma strongly increased the coke-resistant of the catalyst by the electron-impact with catalyst surface. The possible reaction mechanism in the conversion of CH_4 assisted by plasma with or without a catalyst were proposed by a range of catalyst characterizations, product analysis and the plasma kinetic modeling.

2. Experimental

2.1 Synthesis of catalysts

CeO_2 supports and the Pd/CeO_2 catalysts were synthesized by the reported hydrothermal method[39] and deposition-precipitation method,[40] respectively. The detailed synthesis process can be seen in the Supplementary Information.

2.2 Characterization of catalysts

The powder X-ray diffraction (XRD) was performed on a D8 ADVANCE (Bruker, Germany) diffractometer with Cu Kα radiation. The Raman spectra were obtained using a Raman microscope (inVia, RENISHAW, England) system by excitation of the sample at 532 nm with measurement range from 100 to 4,000 cm^{-1}. The high-resolution transmission electron microscopy (HR-TEM) was carried out on a JEM-2100F microscope (Japan) at 200 kV. The high-angle annular dark-field scanning transmission electron micrograph (HAADF-STEM) images and the corresponding elemental mappings were performed on the same instrument. The field-emission scanning electron microscopy (FE-SEM) combined with the energy dispersive X-ray analysis (EDS) was operated on a SIGMA microscope (Zeiss Merlin Compact, Germany). Before the test, the samples were dispersed in the ethanol and then dripped onto aluminum foil to accurately determine the carbon content. All analyzed elements were normalized and the carbon content was tested three times. The N_2 adsorption-desorption measurement was operated at -196 °C on an ASAP 2020HD88 unit (Micromeritics, America) to obtain the specific surface area (S_{BET}) values of each sample. X-ray photoelectron spectroscopy (XPS) was operated with Al Kα radiation (ESCALab-250Xi). The binding energy of all spectra was calibrated using the C1s signal at 284.6 eV. Temperature programmed reduction by hydrogen (H_2-TPR) was carried out on a Micromeritics Autochem II 2920 analyzer with a thermal conductivity detector (TCD). The fresh $0.5Pd/CeO_2$ sample (50 mg) was pretreated in air at 300 °C before the test. Then, the catalyst was heated in 10% H_2/Ar (30 mL min^{-1}) gas mixture from room temperature to 600 °C. Temperature programmed oxidation by oxygen (O_2-TPO) was performed at the same analyser (Micromeritics Autochem II 2920) with a TCD. First, the used samples (100 mg) were activated at 300 °C in He. Then, the samples were heated in 2% O_2/He (30 mL min^{-1}) gas mixture from room temperature to 800 °C. The thermogravimetric (TG) analysis was carried out on a TG-DTA6300 instrument. The sample was treated in air from room temperature to 800 °C (10 °C min^{-1}). The optical emission spectroscopy (OES) from the plasma in the CH_4 DBD reactor was recorded using a spectrograph via an optical fiber equipped with a Princeton Instruments ICCD camera (Andor DH334T) in the range of 300–700 nm. During the test, the optical fiber was placed close to the ground electrode of the DBD reactor. For the spectrometer, the slit width was fixed at 50 μm and the grating groove density was specified to 1,200 mm^{-1}.

2.3 Catalytic tests

The nonoxidative conversion of CH_4 were performed in a DBD reactor as shown in Figure 1, in which the catalytic tests were performed at atmospheric pressure with a catalyst bed in the discharge zone. The reactor was a typical cylindrical DBD quartz tube (14 mm o.d.×10 mm i.d.) reactor, which used a stainless-steel foil covering outside of the quartz tube as the grounding electrode and a stainless-steel rod (6 mm o.d.) placed along the axis of the quartz tube as the high voltage electrode. The quartz tube also served as the dielectric between the high voltage electrode and the grounding electrode. In the reactor, a sieve plate was embedded and used to fix the high voltage electrode. The discharge length of the DBD reactor was 130 mm. The discharge gap was 2 mm. The DBD reactor was connected to a nanosecond pulse power supply (Smart Maple HV-2015, China), which provided a peak voltage of 13 kV and an adjustable frequency. The current and voltage of the external capacitor and the actual applied voltage were detected by a digital oscilloscope (Tektronix, DPO 2024). In the plasma-catalysis test, 0.5 g of catalyst (20–40 mesh) was packed into the discharge area and pure CH_4 was introduced into the DBD reactor with a gas hourly space velocity (GHSV) of 9,800 mL g^{-1} h^{-1}. Prior to the reaction, the catalyst was activated at 980 °C for 30 min in 10% H_2/Ar gas mixture. For the temperature-dependent CH_4 conversion test, the reactor temperature was controlled from 800 to 980 °C. At each temperature, the temperature is constant and the same as the set value. Each reaction was allowed to equilibrate for 1 h and then the concentrations of outlet gases were analyzed. Meanwhile, the experiments were repeated three times and the average of the three measurements was taken. The gaseous products were analyzed via a gas chromatograph (Thermo-Fisher, trace1300) equipped with a thermal conductivity detector (TCD) as well as a flame ionized detector (FID) and calculated by an internal standard method. The TCD with a TDX-01 packed column was used to quantify the CH_4 and H_2. The light hydrocarbons including C_2H_6, C_2H_4, C_3H_8, C_3H_6, C_4H_{10} and C_2H_2 were quantified through the FID with a HPPLOT Al_2O_3 capillary column.

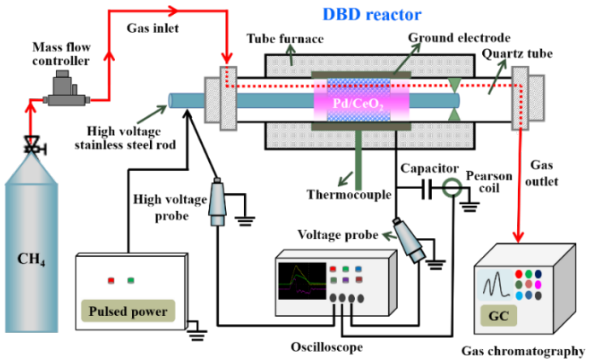

Figure 1. Schematic diagram of the fixed bed DBD reactor setup for the nonoxidative conversion of CH_4.

The calculation on CH_4 conversion (C_{CH4}), hydrocarbon products selectivity (S_{CxHy}) and yields (Y_{CxHy}), H_2 selectivity (S_{H2}) and yield (Y_{H2}), carbon balances (B_C), hydrogen balances (B_H) and energy consumption (EC) of the discharge were shown in the Supplementary Information.

2.4 Density functional theory calculation methods

The Density functional theory (DFT) calculation was applied with Castep program package with the GGA and PW91 functional in the package of Material Studio to simulate the conversion of CH_4.[41, 42] Because of the nonmagnetic properties of Pd, the spin polarization effect was not considered. The convergence criterion for energy, maximum force, stress and energy cutoff were set at 2×10^{-5} eV atom^{-1}, 0.05 eV Å^{-1}, 0.1 GPa and 400 eV, respectively. Density mixing electronic minimizer with a mixing scheme of Pulay was used and the convergence criteria for self-consistent field (SCF) was set as 1.0×10^{-5} eV/atom. The Brillouin zone was sampled by k point of 3×3×1. The transition state (TS) was determined using the LST/QST method.

The Pd (111) surface was modelled by a three-layer slab within a (3×3) super cell (27 Pd atoms in the cell) and the positions of all atoms except for those in the bottom layer were fully relaxed. A vacuum of 10 Å along Z-direction was applied to avoid interactions between periodic images.

Adsorption energy was calculated as

$$E_{ads} = E_{adsorbates/slab} - E_{slab} - E_{adsorbates} \quad (1)$$

Where $E_{adsorbates/slab}$, E_{slab} and $E_{adsorbates}$ are the energies of the surface with the adsorbate molecule, clean surface without any adsorbate and the isolated molecule in the gas phase, respectively.

The activation barrier E_a and reaction energy ΔE are defined as:

$$E_a = E(TS) - E(IS) \quad (2)$$

$$\Delta E = E(FS) - E(IS) \quad (3)$$

Where E(IS), E(TS) and E(FS) refer to the total energies of the initial, transition and final states, respectively.

2.5 Plasma kinetic modelling

A zero-dimensional (0D) plasma kinetic modelling was performed to elucidate the main reaction mechanism in the plasma for the conversion of CH_4 without 0.5Pd/CeO_2. The plasma chemistry consisting of 23 species (i.e., neutrals, radicals and charged species) and 132 reactions together with the corresponding rate coefficients were listed in Table S1 (See the Supplementary Materials). The rate coefficients related to electron-impact reactions were calculated by a Boltzmann solver Bolsig+[43] according to the energy-dependent collision cross sections[44, 45] between electrons and molecules. The rate coefficients of the electron-ion, ion-neutral and neutral-neutral reactions were usually as a function of gas temperature T_g. All species were assumed to be uniform in the reactor. The initial electron density was set to 10^7 cm^{-3}, which is the sum of positive ion densities satisfying the electroneutrality constraint. Besides, the initial densities of the radicals were set to 10^2 cm^{-3}.

The time evolution of the density for all species was formulated as

$$\frac{dN_i}{dt} = \sum^j S_{ij} \quad (4)$$

where subscripts i and j represent ith species and jth reaction, respectively. N_i is the species density and S_{ij} is the source term.

The time evolution of electron energy equation is expressed as

$$\frac{\partial N_\varepsilon}{\partial t} = -e\Gamma_e E - \sum_j \Delta\varepsilon_j r_{inel,j} \quad (5)$$

where N_ε represents the electron energy density, $\Delta\varepsilon_j$ and $r_{inel,j}$ are the energy loss derived from inelastic collisions and the reaction rate in the jth reaction, respectively. Γ_e is electron flux with $\Gamma_e = \mu_e E N_e$, where μ_e is electron mobility, E is electric field, N_e is electron density.

The operating parameters of the simulation used here were the same as those of the experiment (See the catalytic tests section).

3. Results and discussion

3.1 Catalytic performance of the catalysts with the plasma for CH_4 conversion

First, we studied the CH_4 conversion performance and product selectivity of 0.5Pd/CeO_2 at 980 °C. As shown in Figure 2a, for the catalysis-only condition, CH_4 conversion can reach 12.9% at 980 °C, which is much higher than that (4%) for the blank reactor, indicating the crucial catalytic CH_4 activation of the 0.5Pd/CeO_2 catalyst. The selectivity of the light olefins for 0.5Pd/CeO_2 were obviously lower than those for the blank reactor, while the H_2 selectivity was much higher, indicating the presence of the carbon deposition at high temperature. Under the plasma-catalysis condition, CH_4 conversion of Plasma+0.5Pd/CeO_2 (1 kHz) was similar to that of 0.5Pd/CeO_2 without plasma when the discharge power was ca. 13.6 W, indicating that the weak discharge was not efficient for the remove of adsorbed species on the catalyst surface. However, when the discharge power reached ca. 25.1 W, CH_4 conversion over the Plasma+0.5Pd/CeO_2 (3 kHz) was almost doubled from 12.9% to 23.6% (an enhancement of ca. 10.7%) compared with that under the catalysis-only. CH_4 conversion (4.7% vs 4%) over the blank reactor with or without plasma was almost unchanged (Figure 2a). The activity difference over 0.5Pd/CeO_2 and the blank reactor suggests that the role of plasma could not only be related with the gas-phase reaction, but also there could be the existence of plasma-assisted surface reactions, promoting the conversion of CH_4.[46, 47] The waveforms of discharge voltage (U_{total}), gas voltage (U_{gas}), dielectric voltage (U_{diele}) and discharge current (I_{total}) were shown in Figure S1. The similar voltage-current waveforms indicated the same discharge properties, suggesting the stability of the controlled experiment. At the same discharge parameters, The EC for the Catalyst+Plasma is much lower than that for the Blank+Plasma (Table 1), exhibiting the key role of Pd/CeO_2 catalysts in improving the reaction performance. In addition, the stability tests of the catalysts at 980 °C under both

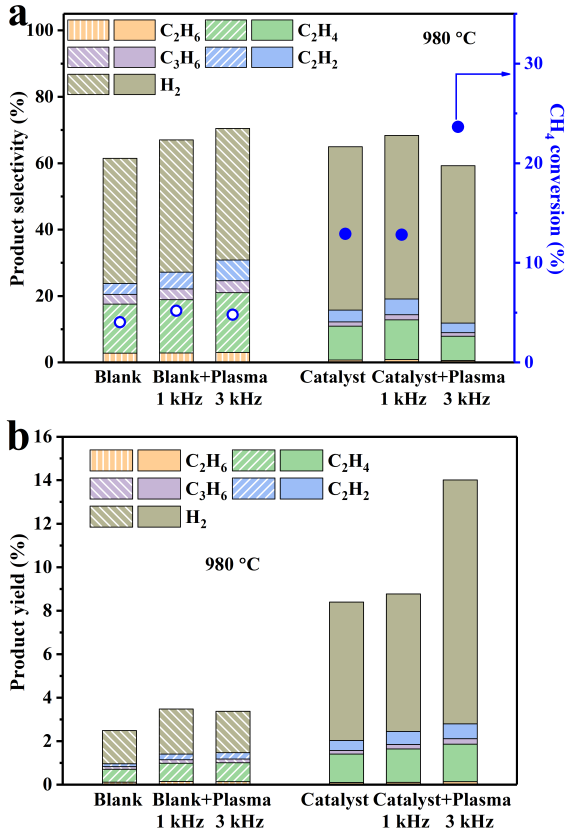

Figure 2. (a) CH_4 conversion, product selectivity and (b) product yield over the 0.5Pd/CeO_2 catalyst in comparison to that over a blank reactor with or without plasma at 980 °C (discharge voltage: 13 kV; frequency: 1 kHz or 3 kHz; rising time: 300 ns; falling time: 500 ns).

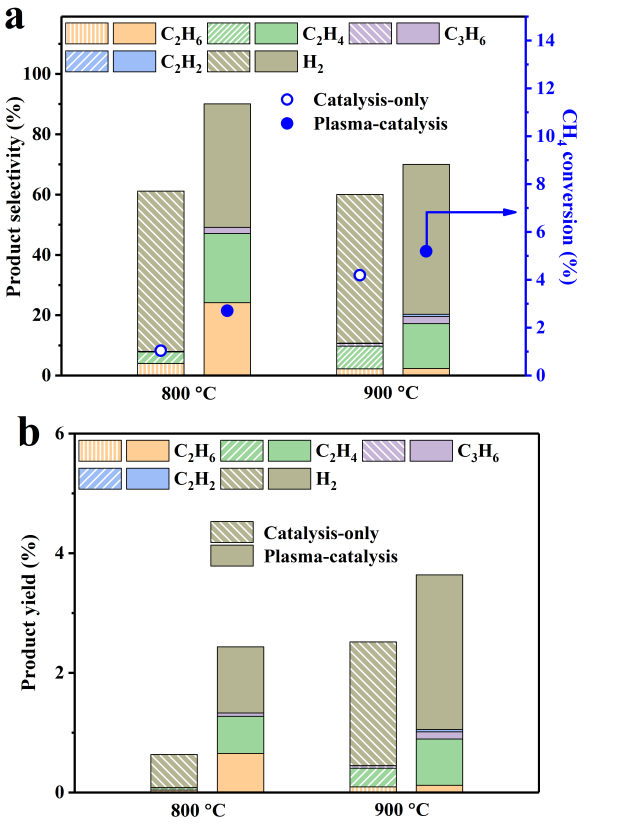

Figure 3. (a) Methane conversion, product selectivity and (b) product yield over the 0.5Pd/CeO_2 catalyst with or without plasma at 800 °C and 900 °C (discharge voltage: 13 kV; frequency: 1 kHz; rising time: 300 ns; falling time: 500 ns).

thermal and

plasma conditions were performed. As shown in Figure S2, the conversion of CH_4 slightly decreased during the 6-h test under both thermal and plasma conditions, indicating the fast formation of carbon under catalysis-only conditions, and the collision between plasma and catalyst can ensure the desorption of CH_3 species from the catalyst surface to suppress the catalyst deactivation in a certain period of time.

The selectivity of each product was similar to that without plasma (Figure 2a), which suggested that the plasma was mainly involved in homogeneous CH_4 activation, and as the initial step of activating CH_4 to form CH_3 radicals, without influence on the subsequent reaction pathway.[46] Notably, the selectivity and the C & H balance for 0.5Pd/CeO_2 with plasma were slightly lower than that for the blank reactor with plasma (Figure 2a and Figure S3a), suggesting the presence of the high carbon hydrocarbons gas (C_{4+}) resulting from further chain growth and cyclization, which were not detected by FID or TCD. Some high carbon hydrocarbon solidifications in the wall of the tube were observed during the test. The yield of each product under the plasma-catalysis condition was more than that for catalysis-only (Figure 2b). For the CeO_2 support (Figure S4), the CH_4 conversion was similar to that for blank reactor (5.5% vs 4%). Moreover, CH_4 conversion increased from 5.5% to 11.3% (an enhancement of ca. 5.8%) after the introduction of plasma, indicating the contribution of plasma could only be in connection with the gas-phase reaction. It also implied the importance of the Pd species in catalytic CH_4 conversion.

To better understand the effect of 0.5Pd/CeO_2 catalyst with or without plasma on CH_4 conversion, we studied CH_4 conversion, product selectivity and yields at lower temperatures. As displayed in Figure 3, CH_4 conversions, the selectivity and yields of the C_2 products under the plasma-catalysis condition increased obviously at 800 °C and 900 °C, which were much higher than those from the blank reactor with plasma (Figure S5). The C & H balance was nearly 100% for the0.5Pd/CeO_2 catalyst with or without plasma at different temperatures (Figure S3b), suggesting that less carbon deposition at lower temperatures. The corresponding voltage-current waveforms of with plasma at 800 °C and 900 °C were

Table 1. Comparison of discharge power (P) and energy consumption (EC) from plasma at 980 °C.

Samples	P (W)	EC (J $mmol^{-1}$)
Blank+Plasma (1 kHz)	8.4	7.6
Blank+Plasma (3 kHz)	17.4	16.9
Catalyst+Plasma (1 kHz)	13.6	4.3
Catalyst+Plasma (3 kHz)	25.1	4.6

Discharge parameter: discharge voltage: 13 kV; frequency: 1 kHz or 3 kHz; rising time: 300 ns; falling time: 500 ns.

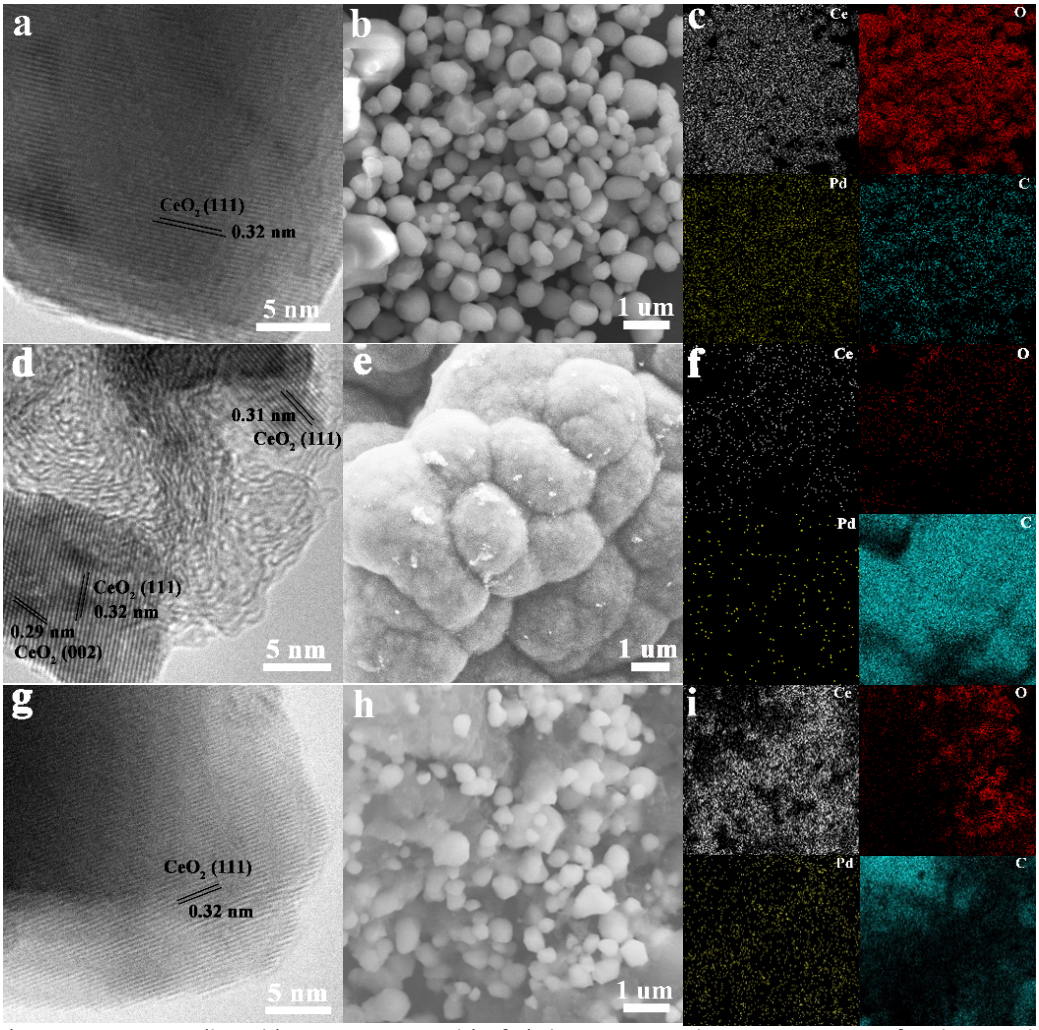

Figure 4. (a, d, g) HR-TEM images, (b, e, h) SEM images and (c, f, i) the corresponding EDS mappings for the 0.5Pd/CeO_2 catalysts: (a–c) the fresh catalyst; (d–f) the catalyst after catalysis-only; (g–i) the catalyst after plasma-catalysis. The collection zones of STEM-EDS elemental mapping images corresponded to the SEM areas.

shown in Figure S6. The CH_4 conversion under the plasma-catalysis condition reached 5.2% at 900 °C, which are quite higher compared with those for the 0.5Pd/CeO_2 catalyst, indicating that the addition of the plasma can promote the conversion of CH_4. The selectivity of C_2H_4 and H_2 reached 15% and 50%, respectively.

In addition, the 0.5Pd/CeO_2 catalyst with plasma showed excellent low-temperature catalytic reactivity. At 800 °C, the CH_4 conversion reached nearly 3%. The onset temperature of CH_4 activation on the 0.5Pd/CeO_2 catalyst with plasma is much lower than that previously reported for single-atom Fe©SiO_2[13] and Pt_1@CeO_2.[14] Table S2 showed the CH_4conversion and the selectivity of C_2 products (C_2H_6, C_2H_4 and C_2H_2) over various catalysts reported from the literature. Although the selectivity of C_2 products was slightly lower than those at higher temperature, the Pd/CeO_2 catalyst with plasma in our work has the competitive CH_4 conversion at lower temperature compared with that reported from the literature. This also provides a promising strategy to achieve the nonoxidative conversion of CH_4 at lower temperatures.

3.2 The effect of plasma on carbon deposited over the catalyst surface

The morphology and the corresponding elemental mapping analysis of the fresh (named as 0.5Pd/CeO_2-fresh) and used 0.5Pd/CeO_2 catalyst without or with plasma (named as 0.5Pd/CeO_2-used and Plasma+0.5Pd/CeO_2-used, respectively) were characterized. The fresh 0.5Pd/CeO_2 catalyst calcined at 980 °C underwent severe sintering compared with the rod-like CeO_2 supports subjected to the calcination at 400 °C (Figure 4a, b and Figure S7 and S8a). The 0.5Pd/CeO_2 catalyst sintered into irregular shapes with a size of 200 nm or more. No palladium-containing phases were observed, indicating the stable Pd species disperse uniformly on CeO_2. Only the clear interplanar spacing of 0.32 nm was detected (Figure 4a and Figure S8d), corresponding to the (111) lattice fringes of CeO_2.[48] In addition, the elemental mapping analysis confirmed the homogeneous

distribution of both Pd and Ce species (Figure 4b, c). Notably, a small quantity of carbon species was also detected (6.8%, Table 2), which mainly resulted from the surface-adsorption carbonaceous species.[35]

Under catalysis-only condition, except the (111) and (002)[48] lattice fringes of CeO_2, large amounts of carbon species over the catalyst were observed (Figure 4d–f and Figure S8b, e). Furthermore, only weak Ce, O and Pd signals were detected (Figure 4e, f). The carbon species were typical of amorphous carbon and had limited order due to the absence of the observable graphitic reflections in XRD or the HR-TEM.[49] However, under plasma-catalysis condition, besides the distribution of carbon element, the signals of Ce, O and Pd elements were obvious (Figure 4g–i), indicating that the introduction of plasma can effectively inhibit the degree of the carbon deposition. The quantification of the carbon element from the EDS results also verified this point (Table 2). The carbon content (31.0%) under plasma-catalysis condition was much lower than that (100.0%) under catalysis-only condition (Table 2). To better exhibit the distribution of Pd species, HAADF-STEM images and the corresponding elemental mappings were performed. The active Pd species were approximately isolated and monodispersed on CeO_2 (Figure S9). In a word, the addition of the plasma can effectively reduce the amount of the carbon deposition. Further, CeO_2 as support can effectively suppress the aggregation of Pd species during the high-temperature catalytic reaction, showing the outstanding heat resistance and structure stability.

The specific surface areas (S_{BET}) of the samples were measured by N_2 adsorption-desorption isotherms and the corresponding results were summarized in Table 2. The CeO_2 support showed relatively high S_{BET} at ca. 77 $m^2\ g^{-1}$. However, the S_{BET} value decreased seriously to 0.19 $m^2\ g^{-1}$ for the fresh 0.5Pd/CeO_2 calcined at 980 °C, mainly due to the increasing

Table 2. Physicochemical properties of the catalysts.

Samples	Raman intensity I_D/I_G	Carbon content (%)[a]	Carbon amount (wt%)[b]	S_{BET} ($m^2\ g^{-1}$)[c]
CeO_2	–	–	–	77
0.5Pd/CeO_2-fresh	–	6.8	–	0.19
0.5Pd/CeO_2-used	1.56	100.0	48.0	3.49
Plasma+0.5Pd/CeO_2 -used	1.54	31.0	36.3	0.31

[a] determined by SEM-EDS. [b] calculated from TGA. [c] BET surface area of samples.

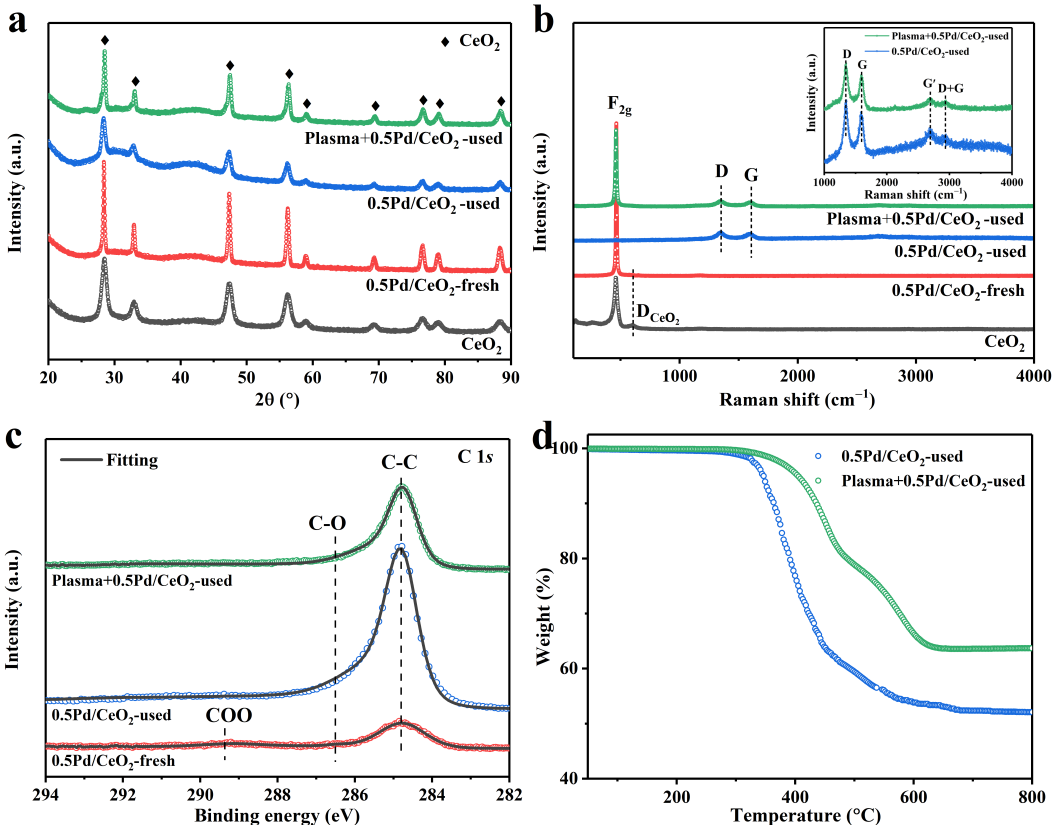

Figure 5. (a) XRD patterns and (b) Raman spectra of the CeO_2 support, the fresh and used 0.5Pd/CeO_2 catalyst with or without plasma. (c) XPS spectra of C 1*s* for the fresh 0.5Pd/CeO_2, the used 0.5Pd/CeO_2 and Plasma+0.5Pd/CeO_2. (d) TGA profiles of the used 0.5Pd/CeO_2 and Plasma+0.5Pd/CeO_2 following the long-term stability tests.

CeO_2 crystallite size, verified by the SEM images. After the CH_4 conversion, the S_{BET} value (3.49 m^2 g^{-1}) increased evidently, much higher than that (0.31 m^2 g^{-1}) for the used Plasma+0.5Pd/CeO_2, which was mainly attributed to the more carbon deposition on used 0.5Pd/CeO_2.

XRD results showed that all the diffraction peaks for the measured samples could be assigned to the face-centered cubic CeO_2 (JCPDS 34-394) phase (Figure 5a). No diffraction peaks could be consistent with the Pd species, possibly due to the low loading of Pd species. It also suggested the small particle size and high dispersion of the Pd species on CeO_2 support, which was in line with the HAADF-STEM results. In addition, the mean crystallite sizes (*d*) of the samples were calculated according to Scherrer equation, which were summarized in Table S3. The 0.5Pd/CeO_2-fresh calcined at 980 °C became much larger compared with CeO_2 supports subjected to the calcination at 400 °C (24.9 nm vs 8.8 nm). However, the mean crystallite sizes of CeO_2 obviously decreased for the used 0.5Pd/CeO_2 with or without plasma. Moreover, the size of CeO_2 for the used Plasma+0.5Pd/CeO_2 was apparently larger compared with that for the used 0.5Pd/CeO_2 (Table S3). This can be due to the less carbon deposition and more exposure to CeO_2 after the introduction of the plasma. These phenomena well supported the interpretation of the SEM images.

Raman spectra tests were used to investigate the surface specific structure of the catalysts. As shown in Figure 5b, for the fresh 0.5Pd/CeO_2, except the F_{2g} mode (462 cm^{-1}) and the defect-induced (D_{CeO2}, 601 cm^{-1}) mode of the cubic CeO_2 fluoride phase,[48, 35] no peaks related to the Pd species were detected, suggesting the small size and low loading of Pd species. For the used 0.5Pd/CeO_2 catalyst, there was the presence of four new peaks. The strong peak at 1,349 cm^{-1} was assigned to the disorder in graphitic carbon denoted as D.[50] The G-band at 1,596 cm^{-1} and the G'-band at 2,694 cm^{-1} were ascribed to the graphitic in-plane stretching vibrations from sp^2-bonded carbon and 2D vibrations,[51, 52] respectively. The presence of the G-band demonstrated the existence of graphitic carbon.[53] The weak G'-band represented the short-range honeycomb structure, indicating the partially order carbon structure.[49] Another weak peak at 2,932 cm^{-1} was assigned to the combination of G and D.[52] However, no peaks were assigned to the CeO_2 fluoride phase and Pd species, suggesting that the deposition of carbon species covered the catalyst signal. Surprisingly, the peak related to the F_{2g} mode of ceria was detected for the used Plasma+0.5Pd/CeO_2, indicating that the degree of the carbon deposition can be effectively weakened after the introduction of plasma. The similar I_D/I_G ratios (Table 2) between used 0.5Pd/CeO_2 and Plasma+0.5Pd/CeO_2 suggested the same graphitic structure, indicating that the addition of plasma did not change the structure of the 0.5Pd/CeO_2 catalyst.

Figure 5c and Figure S10 showed the XPS spectra of C 1*s*, Pd 3*d*, Ce 3*d* and O 1*s* for the 0.5Pd/CeO_2 samples. For Pd 3*d* XPS spectrum of the fresh 0.5Pd/CeO_2 (Figure S10a), two symmetric peaks at 337.5 eV and 342.8 eV corresponded to highly dispersed Pd species in the Pd^{2+} state.[54] However, for the used Plasma+0.5Pd/CeO_2 (Figure S10a), the accurate confirmation of the Pd species was difficult due to the poor

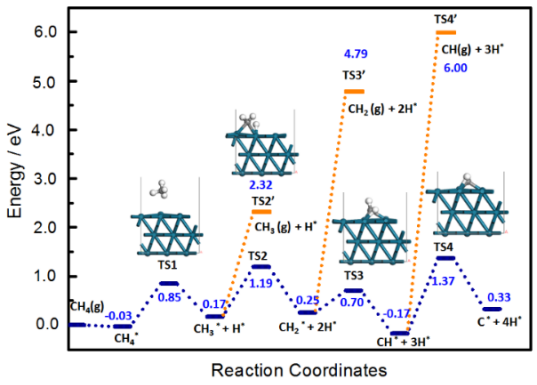

Figure 6. CH_4 consecutive dehydrogenation pathways (blue lines) and desorption energy of reaction intermediates (orange lines) on Pd-site based on DFT simulations.

noise resulting from the lower Pd content covered partially by the carbon. From H_2-TPR results (Figure S11), PdO species highly dispersed were easily reduced below 200 °C,[55] while the reduction of PdO species interacting strongly with CeO_2 can be reduced below 400 °C.[55] Thus, the active state of 0.5Pd/CeO_2 was metallic Pd phase.

To explore the coordination structure of carbon species, C 1*s* XPS spectra were studied (Figure 5c). For the fresh sample, the peak at 284.8 eV can be assigned to the C-C bond from graphitized carbon.[56] Two weak peaks at 286.5 eV and 289.2 eV were related to the C-O bond and COO bond,[56, 57] respectively. These bonds may result from the contaminant carbon of the measurement system[58] or the adsorption of CO_2 and H_2O in the air. For the used 0.5Pd/CeO_2 and Plasma+0.5Pd/CeO_2, they showed the same coordination structure of carbon. The peak intensity related to the C-C bond increased, confirming the deposition of carbonaceous species during CH_4 conversion. The C-O bond still existed, primarily from the CO_2 adsorption in air. Notably, the peak intensity of C-C bond for the used 0.5Pd/CeO_2 was much higher compared with the used Plasma+0.5Pd/CeO_2. Besides, for the XPS spectra of Pd 3*d*, Ce 3*d* and O 1*s* (Figure S10), the peak intensity of the fresh 0.5Pd/CeO_2 was much stronger than that of the used Plasma+0.5Pd/CeO_2. These observations are accordance with the Raman and SEM results. The amount of carbon deposition can be effectively reduced after the addition of plasma.

The contents and types of the deposited carbon were characterized by TGA and O_2-TPO. As summarized in Table 2, TGA results showed that the used Plasma+0.5Pd/CeO_2 possessed a totally weight reduction of 36.3 wt%, in agreement with the SEM-EDS data (Table 2). Meanwhile, more carbon content (48.0 wt%) for the used 0.5Pd/CeO_2 were detected. While, this value was much lower than the SEM-EDS results (ca. 100%). This is due to that the large amounts of carbon covered over the catalyst, and the thickness of carbon reached the lower detection limit of the SEM instrument, so that weak catalyst information was detected, leading to higher carbon content. In addition, they showed the similar TGA and O_2-TPO profiles (Figure 5d and Figure S12), confirming the same types of the deposited carbon. The weight loss between 380 and 520 °C was ascribed to amorphous carbon and the weight loss between 520 and 720 °C corresponded to filamentary carbon.[59, 60] The weight loss at more than 720 °C resulted from the burn-off of graphitic

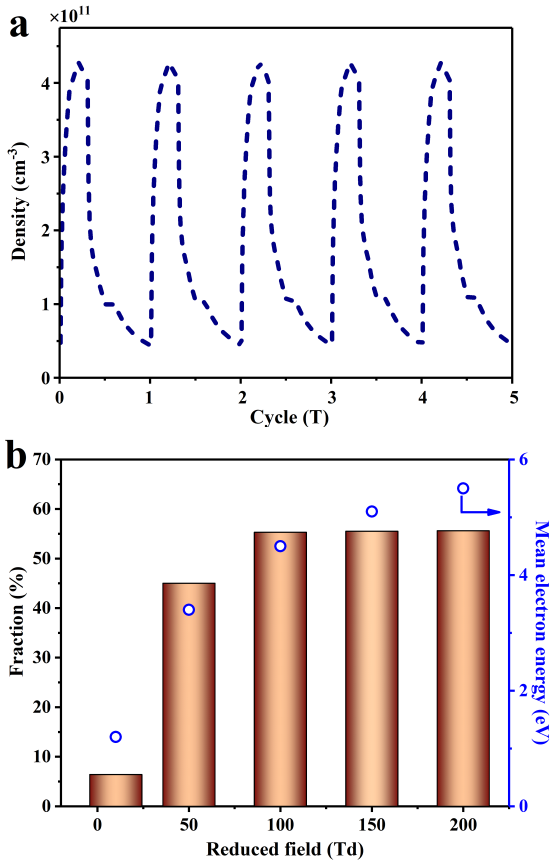

Figure 7. (a) The density of the electron as a function of time for the CH_4 conversion assisted by plasma without catalyst. (b) The ratio of the electron and mean electron energy as a function of reduced field under the plasma-only conditions.

carbon, which was difficult to gasify or removed by regeneration.[59] These carbon species were responsible for the low catalytic activation of 0.5Pd/CeO_2.

3.3 Reaction mechanism of the catalysts with the plasma for CH_4 conversion

To identify the active species of the plasma-catalysis condition during the conversion of CH_4, the OES measurement was performed. As shown in Figure S13, the excited CH ($C^2\sum^+ \rightarrow X^2\prod$), CH ($A^2\Delta \rightarrow X^2\prod$) and C_2 ($d^3\prod \rightarrow a^3\prod$) bands were identified in the OES spectra,[61] demonstrating the existence of CH radicals. This also indicates the presence of CH_3 and CH_2 radicals because the CH radicals are generated via the progressive dehydrogenation of CH_4 under the plasma condition.[62] Two CH_3 radicals coupled and further reacted with other active species to generate other products. The rest of peaks were assigned to the vibration of the N_2 and N_2^+,[63, 64] which mainly resulted from the discharge between the ground electrode and the quartz tube. The bands assigned to the CH and C_2 were very weak compared with those from the N_2 and N_2^+. It was mainly because that the size (20–40 mesh) and voids of the catalyst were very small, leading to the light from the CH_4 discharge were obscured.

The DFT calculations were carried out to explore the reaction mechanism and understand the reason of carbon deposition on 0.5Pd/CeO_2 without plasma. The Pd (111) surface was

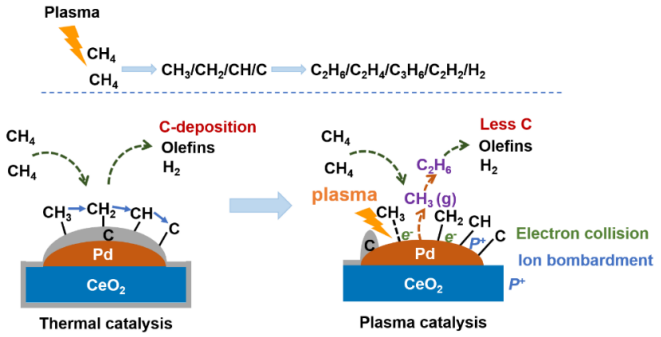

Figure 8. Proposed reaction mechanisms on the Pd/CeO_2 surface for the direct conversion of CH_4 with the thermal catalysis and plasma catalysis methods.

constructed to adsorb CH_4, which was easily activated to generate adsorbed CH_3 (0.88 eV, Figure 6). However, the consequent dehydrogenation of the adsorbed CH_3 ($CH_3^* \rightarrow CH_2^*+H^*$) on the catalyst surface is much favorable compared with the desorption (1.02 eV vs 2.15 eV). The adsorbed CH_4 mainly occurred consecutive dehydrogenation steps on Pd-site, finally formed the carbon deposition. Therefore, the conversion of CH_4 on Pd-site tends to form carbon-coking, leading to a large amount of carbon covered the catalyst surface, lowering the catalytic performance. Notably, the desorption of the adsorbed CH_3 was easier than that of the adsorbed CH_2 and CH.

After the introduction of plasma, CH_4 molecules were cracked to generate the abundant CH_3 radicals, two CH_3 radicals coupled easily to generate the C_2H_6. If the CH_3 radicals can readily react with the adsorbed CH_3 to generate the C_2H_6, we also simulated the steps via DFT. As shown in Figure S14, the energy that the CH_3 radicals reacting with the adsorbed CH_3 to generate the C_2H_6 was ca. 2.76 eV, suggesting the difficult process. It also indicated that the conversion of CH_4 to hydrocarbons could occur firstly through desorption of adsorbed CH_3 from the surface of catalyst to form CH_3 radicals, and then the CH_3 radical reacted with the gaseous molecules.

According to product analysis and a range of catalyst characterizations, it can be concluded that there is the serious carbon deposition over only 0.5Pd/CeO_2. However, the amount of carbon deposition is greatly reduced after the addition of plasma. The influence of plasma on carbon deposition have been discussed in detail. Firstly, the intense electric field and the diffusion of the active species generated by plasma could modify the surface charge transfer and work function of catalysts to promote the desorption of CH_3.[65, 66] Secondly, the energized electron and ions generated by plasma could impact with adsorbed CH_3 species, which could accelerate CH_3 species to desorb from the catalyst surface, reducing the amount of carbon deposition. The density of electron averaged over one period was ca. 10^{11} cm^{-3} (Figure 7a). The desorption of adsorbed CH_3 species needed at least 2.15 eV (Figure 6). Thus, the electron ratio in the range from 2 eV to 9 eV (the minimum

energy threshold of CH_4 dissociation and ionization collision) was calculated, which enabled the adsorbed CH_3 to desorb. As shown in Figure 7b, there was about 55% of the electrons in the 2–9 eV energy range when the reduced field intensity was more

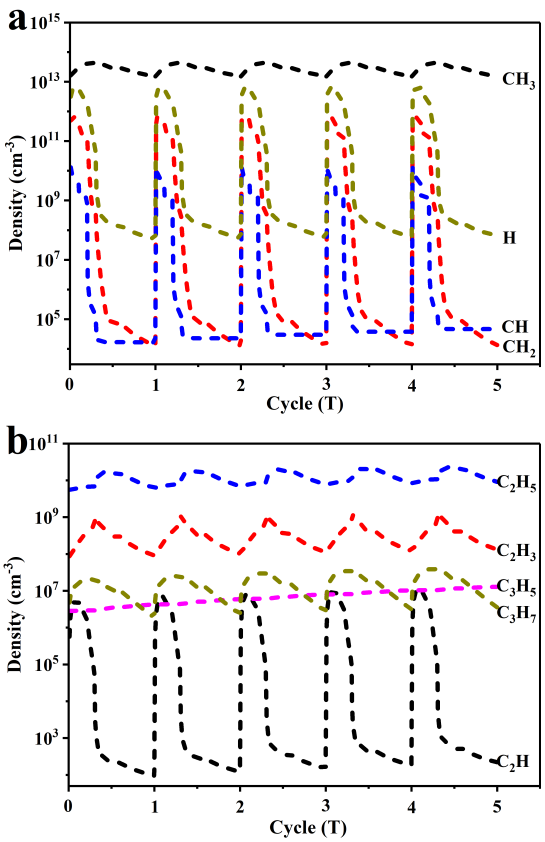

Figure 9. The density of each radical as a function of time during five periods for the CH_4 conversion assisted by plasma without catalyst.

than 100 Td. Although not all of the electrons participated in the desorption of CH_3, a part of electrons > 2 eV provided the possibility in CH_3 desorption from catalyst surface into gaseous phase, inhibiting the progressive dehydrogenation of adsorbed CH_3.

Combining the above analysis with previous study,[13] we infer that the reaction mechanism of CH_4 conversion assisted by plasma in nonoxidation condition is that CH_4 was firstly activated by the Pd-site to form the adsorbed CH_3. Partial adsorbed CH_3 bombarded by plasma can desorb from the Pd-site to form the CH_3 radical. Two CH_3 radicals were coupled to form C_2H_6. The forming C_2H_6 species subsequently underwent dehydrogenation and recombination reactions in the gas phase to generate C_2H_4 and other hydrocarbons. The proposed reaction mechanisms on the Pd/CeO_2 surface for the direct conversion of CH_4 into olefins and H_2 with the thermal catalysis and plasma catalysis methods were displayed in Figure 8.

3.4 Plasma kinetic modeling

Plasma kinetic modeling based on a zero-dimensional model was performed to study the possible reaction pathways in the plasma for the CH_4 conversion without $0.5Pd/CeO_2$ catalyst. The operating parameters of the simulation used here were the same as those of the experiment (See catalytic tests section). The simulation results were obtained under the condition of 800 °C and 760 Torr. Figure 9 showed the densities of radicals as a function of time for five periods. The densities of the radicals exhibited the similar periodic behaviour. The density of each radical continuously increased during the pulse duration and gradually decreased during the pulse-off period, indicating that the generation of hydrocarbons and H_2 mainly occurred in the gas phase through the recombination of the radicals during the pulse-off period. Besides, the densities of radicals averaged over one period were calculated and the most abundant radical was CH_3 (10^{13} cm^{-3}), followed by H, CH_2, C_2H_5, CH, and C_2H_3.

Figure S15 displayed the densities of CH_4 and the gas products as a function of time. The density of CH_4 was initially 6.84×10^{18} cm^{-3}, which decreased gradually due to the dissociation and ionization reactions to generate various radicals. Subsequently, hydrocarbons such as C_2H_6, C_2H_4, C_2H_2, C_3H_6 and H_2 formed via the recombination of the radicals. The rapid growth of the densities for the products appeared within the first 0.5 s. subsequently, the growth of got slow, and finally did not significantly change. A residence time of 4.8 s was calculated. H_2 was formed with the highest density at 4.8 s. The densities of C_2H_6 and C_2H_4 were in the order of 10^{16} cm^{-3}, which is one order of magnitude higher than that for C_2H_2 and C_3H_6.

The CH_4 conversion, selectivity of major products and C & H balance based on the above calculation for particle densities were displayed in Figure S16a. The calculated CH_4 conversion and products selectivity at 4.8 s matched well with the experimental results (Table S4), further verifying the reliability of the model. The kinetic simulation for CH_4 pyrolysis in the blank reactor were also studied. As displayed in Figure S17, the change trends based on CH_4 conversion and products selectivity were accordance with those from CH_4 conversion assisted by plasma without catalyst (Figure S16a). The thermal cracking of CH_4 was consecutive dehydrogenation processes. Each free radical reacted to form the final products.

To explore the underlying mechanism governing CH_4 conversion activated by plasma, the generation and loss rates of each product were presented in Figure S16b–f. The reaction mechanism of CH_4 conversion assisted by plasma was obviously different from that of CH_4 pyrolysis. As summarized in Figure S18. Firstly, CH_4 molecules were dissociated to form CH_3, CH_2, CH and H radicals with electron. Subsequently, two CH_3 radicals combined or CH_4 reacted with CH_2 to form C_2H_6. C_2H_6 was readily dehydrogenative, followed by a series of gas-phase reaction to form various light hydrocarbon. Besides, the CH_3 radicals could activate CH_4 homogeneously to enhance the CH_4 conversion (R38, Table S1) and CH_4 could react with H radicals to produce the CH_3 radicals (R37, Table S1). Thus, the cycle process promoted the conversion of CH_4, also explaining the reason of the highest density of CH_3 radicals (Figure 9).

4. Conclusions

In summary, we successfully prepared the stable and highly dispersed Pd species on CeO_2. The Pd species interact strongly with the CeO_2 support, efficiently preventing the Pd species from aggregation during high-temperature catalytic test. The

Pd/CeO_2 catalyst assisted by the NTP showed the obvious promotion effect for conversion of CH_4 compared with thermal-catalysis. The introduction of plasma is not only able to activate the C-H bond of CH_4 to dehydrogenation, but also effectively enhance the coke-resistance of the catalyst. This combination of plasma and catalyst offers a new guidance for lowering the activate temperature of CH_4 and the carbon deposition to achieve conversion of methane into high value-added chemicals.

Author Contributions

Xiucui Hu: conceptualization; investigation; formal analysis; writing-original draft. Yadi Liu: software; resources; data curation; formal analysis; visualization. Liguang Dou: visualization, software, resources. Cheng Zhang: validation; visualization. Shuai Zhang: resources; data curation. Yuan Gao: visualization. Xin Tu: supervision; writing-review&editing. Tao Shao: project administration; funding acquisition; supervision.

Conflicts of interest

There are no conflicts to declare.

Acknowledgements

This work is financially supported by the National Science Fund for Distinguished Young Scholars [grant number 51925703], the National Natural Science Foundation of China [grant numbers 51637010, 51807190, 52007178]. We acknowledge the National Supercomputing Center in Shenzhen for providing the computational resources and the software. We thank the Dr. Xiaoyang Cui for the help on the SEM characterizations.

Notes and references

1 Z. Li, Q. Lin, M. Li, J. Cao, F. Liu, H. Pan, Z. Wang and S. Kawi, *Renew. Sust. Energ. Rev.*, 2020, **134**, 110312.
2 S. Wu, X. Tan, J. Lei, H. Chen, L. Wang and J. Zhang, *J. Am. Chem. Soc.*, 2019, **141**, 6592–6600.
3 S. D. Senanayake, J. A. Rodriguez and J. F. Weaver, *Acc. Chem. Res.*, 2020, **53**, 1488–1497.
4 C. Zhang, C. Ren, S. Zhang, H. Xue, Y. Zhao, Z. Zhou, J. Chen, Z. Luo, W. Sang, L. Jing, Y. Teng, Q. Qiu, C. Zhang, M. Gong, G. Zhang, T. Shao and L. Xiao, *Energ. Fuel.*, 2021, **35**, 13930–13936.
5 S. Mehla, A. E. Kandjani, R. Babarao, A. F. Lee, S. Periasamy, K. Wilson, S. Ramakrishna and S. K. K. Bhargava, Energy Environ. Sci., 2020, DOI: 10.1039/D0EE01882A.
6 H. M. Torres Galvis, J. H. Bitter, T. Davidian, M. Ruitenbeek, A. I. Dugulan and K. P. de Jong, *J. Am. Chem. Soc.*, 2012, **134**, 16207–16215.
7 G. H. Torres, J. H. Bitter, C. B. Khare, M. Ruitenbeek, A. I. Dugulan and K. P. de Jong, *Science*, 2012, **335**, 835–838.
8 P. Tian, Y. Wei, M. Ye and Z. Liu, *ACS Catal.*, 2015, **5**, 1922–1938.
9 J. Xu, Y. Zhang, X. Xu, X. Fang, R. Xi, Y. Liu, R. Zheng and X. Wang, *ACS Catal.,* 2019, **9**, 4030–4045.
10 P. Chawdhury, K. V. S. S. Bhargavi and C. Subrahmanyam, *Sustain. Energ. Fuels*, 2021, **5**, 3351–3362.
11 S. H. Morejudo, R. Zanón, S. Escolástico, I. Yuste-Tirados, H. Malerød-Fjeld, P. K. Vestre, W. G. Coors, A. Martínez, T. Norby, J. M. Serra and C. Kjølseth, *Science*, 2016, **353**, 563–566.
12 I. Julian, M. B. Roedern, J. L. Hueso, S. Irusta, A. K. Baden, R. Mallada, Z. Davis and J. Santamaria, *Appl. Catal. B*, 2020, **263**, 118360.
13 X. Guo, G. Fang, G. Li, H. Ma, H. Fan, L. Yu, C. Ma, X. Wu, D. Deng, M. Wei, D. Tan, R. Si, S. Zhang, J. Li, L. Sun, Z. Tang, X. Pan and X. Bao, *Science*, 2014, **344**, 616–619.
14 P. Xie, T. Pu, A. Nie, S. Hwang, S. C. Purdy, W. Yu, D. Su, J. T. Miller and C. Wang, *ACS Catal.*, 2018, **8**, 4044–4048.
15 A. L. Dipu, S. Ohbuchi, Y. Nishikawa, S. Iguchi, H. Ogihara and I. Yamanaka, *ACS Catal.*, 2019, **10**, 375–379.
16 P. Schwach, X. Pan and X. Bao, *Chem. Rev.*, 2017, **117**, 8497–8520.
17 Z. Liu, E. Huang, I. Orozco, W. Liao, R. M. Palomino, N. Rui, T. Duchoň, S. Nemšák, D. C. Grinter, M. Mahapatra, P. Liu, J. A. Rodriguez and S. D. Senanayake, *Science*, 2020, **368**, 513–517.
18 T. Shao, R. Wang, C. Zhang and P. Yan, *High volt.*, 2018, **3**, 14–20.
19 S. Xu, S. Chansai, C. Stere, B. Inceesungvorn, A. Goguet, K. Wangkawong, S. F. R. Taylor, N. Al-Janabi, C. Hardacre, P. A. Martin and X. Fan, *Nat. Catal.*, 2019, **2**, 142–148.
20 X. Chen, S. Zhang, S. Li, C. Zhang, J. Pan, A. B. Murphy and T. Shao, *Sustain. Energ. Fuels*, 2021, **5**, 787–800
21 Y. Gao, S. Zhang, H. Sun, R. Wang, X. Tu and T. Shao, *Appl. Energ.*, 2018, **226**, 534–545.
22 S. Van Alphen, F. Jardali, J. Creel, G. Trenchev, R. Snyders and A. Bogaerts, *Sustain. Energ. Fuels*, 2021, **5**, 1786–1800.
23 C. Xu and X. Tu, *J. Energy Chem.*, 2013, **22**, 420–425.
24 J. Kim, J. Jeoung, J. Jeon, J. Kim, Y. S. Mok and K. Ha, *Chem. Eng. J.*, 2019, **377**, 119896.
25 H. Sun, S. Zhang, Y. Gao, B. Huang, C. Zhang and T. Shao, *Plasma Process. Polym.*, 2019, **16**, 1900050.
26 E. Delikonstantis, E. Igos, M. Augustinus, E. Benetto and G. D. Stefanidis, *Sustain. Energ. Fuels*, 2020, **4**, 1351–1362.
27 X. Li, C. Lin, C. Shi, Y. Xu, Y. Wang and A. Zhu, *J. Phys. D: Appl. Phys.*, 2008, **41**, 175203.
28 J. Bae, M. Lee, S. Park, M. Jeong, D. Hong, Y. D. Kim, Y. Park and Y. K. Hwang, *Catal. Today*, 2017, **293–294**, 105–112.
29 A. Beloqui Redondo, E. Troussard and J. A. van Bokhoven, *Fuel Process. Technol.*, 2012, **104**, 265–270.
30 I. Julian, H. Ramirez, J. L. Hueso, R. Mallada and J. Santamaria, *Chem. Eng. J.*, 2019, **377**, 119764.
31 A. H. Khoja, M. Tahir and N. A. S. Amin, *Energ. Convers. Manage.*, 2019, **183**, 529–560.
32 Z. Guo, Y. Yi, L. Wang, J. Yan and H. Guo, *ACS Catal.*, 2018, **8**, 10219–10224.
33 B. Huang, C. Zhang, H. Bai, S. Zhang, K. K. Ostrikov and T. Shao, *Chem. Eng. J.*, 2020, **396**, 125185.
34 M. Janda, V. Martišovitš, A. Buček, K. Hensel, M. Molnár and Z. Machala, *J. Phys. D: Appl. Phys.*, 2017, **50**, 425207.
35 Z. Hu, X. Liu, D. Meng, Y. Guo, Y. Guo and G. Lu, *ACS Catal.*, 2016, **6**, 2265–2279.
36 X. Hu, X. Fu, W. Wang, X. Wang, K. Wu, R. Si, C. Ma, C. Jia and C. Yan, *Appl. Catal. B*, 2020, **268**, 118424.
37 W. Yu, W. Wang, S. Li, X. Fu, X. Wang, K. Wu, R. Si, C. Ma, C. Jia and C. Yan, *J. Am. Chem. Soc.*, 2019, **141**, 17548–17557.
38 T. P. Senftle, A. C. T. van Duin and M. J. Janik, *ACS Catal.*, 2017, **7**, 327–332.
39 H. Mai, L. Sun, Y. Zhang, R. Si, W. Feng, H. Zhang, H. Liu and C. Yan, *J. Phys. Chem. B*, 2005, **109**, 24380–24385.
40 H. Jeong, J. Bae, J. W. Han and H. Lee, *ACS Catal.,* 2017, **7**, 7097–7105.
41 L. Dou, M. Fu, Y. Gao, L. Wang, C. Yan, T. Ma, Q. Zhang and X. Li, *Fuel*, 2021, **283**, 118984.
42 J. P. Perdew, J. A. Chevary, S. H. Vosko, K. A. Jackson, M. R. Pederson, D. J. Singh and C. Fiolhais, *Phy. Rev. B*, 1992, **46**, 6671–6687.

43 G. J. M. Hagelaar and L. C. Pitchford, *Plasma Sources Sci. T.*, 2005, **14**, 722–733.
44 R. K. Janev and D. Reiter, *Phys. Plasmas*, 2002, **9**, 4071–4081.
45 R. K. Janev and D. Reiter, *Phys. Plasmas*, 2004, **11**, 780–829.
46 J. Hao, P. Schwach, G. Fang, X. Guo, H. Zhang, H. Shen, X. Huang, D. Eggart, X. Pan and X. Bao, *ACS Catal.*, 2019, **9**, 9045–9050.
47 L. Wang, Y. Yi, H. Guo and X. Tu, *ACS Catal.*, 2017, **8**, 90–100.
48 W. Wang, W. Yu, P. Du, H. Xu, Z. Jin, R. Si, C. Ma, S. Shi, C. Jia and C. Yan, *ACS Catal.*, 2017, **7**, 1313–1329.
49 H. A. Calderon, A. Okonkwo, I. Estrada-Guel, V. G. Hadjiev, F. Alvarez-Ramírez and F. C. Robles Hernández, *Adv. Struct. Chem. Imag.*, 2016, **2**, 1–12.
50 K. Han, W. Yu, L. Xu, Z. Deng, H. Yu and F. Wang, *Fuel*, 2021, **291**, 120182.
51 A. K. Hill and L. Torrente-Murciano, *Appl. Catal. B,* 2015, **172–173**, 129–135.
52 Y. A. Kim, K. Fujisawa, H. Muramatsu, T. Hayashi, M. Endo, T. Fujimori, K. Kaneko, M. Terrones, J. Behrends, A. Eckmann, C. Casiraghi, K. S. Novoselov, R. Saito and M. S. Dresselhaus, *ACS Nano*, 2012, **6**, 6293–6300.
53 A. Ferrari and J. Robertson, *Phys. Rev. B,* 2000, **61**, 14095–14107.
54 S. Hinokuma, H. Fujii, M. Okamoto, K. Ikeue and M. Machida, *Chem. Mater.*, 2010, **22**, 6183–6190.
55 G. Ercolino, P. Stelmachowski, G. Grzybek, A. Kotarba and S. Specchia, *Appl. Catal. B* 2017, **206**, 712–725.
56 X. Jia, Y. Dong, X. Li, H. Yu, T. Ma, W. Zhang and H. Dong, *Appl. Surf. Sci.*, 2020, **517**, 146207.
57 Q. Yang, C. Zhou, J. Ni and X. Guan, *Sustain. Energ. Fuels*, 2020, **4**, 2768–2774.
58 Q. Zhao, Y. Wang, Y. Wang, L. Li, W. Zeng, G. Li and C. Hu, *Int. J. Hydrogen Energ.,* 2020, **45**, 14281–14292.
59 Z. Xie, B. Yan, S. Kattel, J. H. Lee, S. Yao, Q. Wu, N. Rui, E. Gomez, Z. Liu, W. Xu, L. Zhang and J. G. Chen, *Appl. Catal. B*, 2018, **236**, 280–293.
60 A. Wang, J. H. Harrhy, S. Meng, P. He, L. Liu and H. Song, *Energ. Convers. Manage.*, 2019, **191**, 93–101.
61 X. Wang, Y. Gao, S. Zhang, H. Sun, J. Li and T. Shao, *Appl. Energ.*, 2019, **243**, 132–144.
62 Y. Yi, X. Wang, A. Jafarzadeh, L. Wang, P. Liu, B. He, J. Yan, R. Zhang, H. Zhang, X. Liu, H. Guo, E. C. Neyts and A. Bogaerts, *ACS Catal.*, 2021, **11**, 1765–1773.
63 Y. Li, D. Yang, J. Qiao, L. Zhang, W. Wang, Z. Zhao, X. Zhou, H. Yuan and W. Wang, *Plasma Sources Sci. T.*, 2020, **29**, 55004.
64 H. Wang, D. Yang, Q. Xu, H. Yuan, X. Zhou and W. Wang, *J. Phys. D: Appl. Phys.,* 2021, **54**, 025202.
65 L. Y. Jia, A. Farouha, L. Pinard, S. Hedan, J. D. Comparot, A. Dufour, K. Ben Tayeb, H. Vezin and C. Batiot-Dupeyrat, *Appl. Catal. B*, 2017, **219**, 82–91.
X. Zhang, Y. Liu, M. Zhang, T. Yu, B. Chen, Y. Xu, M. Crocker, X. Zhu, Y. Zhu, R. Wang, D. Xiao, M. Bi, D. Ma and C. Shi, *Chem*, 2020, **6**, 3312–3328.

References

1 Z. Li, Q. Lin, M. Li, J. Cao, F. Liu, H. Pan, Z. Wang and S. Kawi, *Renew. Sust. Energ. Rev.*, 2020, **134**, 110312.
2 S. Wu, X. Tan, J. Lei, H. Chen, L. Wang and J. Zhang, *J. Am. Chem. Soc.*, 2019, **141**, 6592-6600.
3 S. D. Senanayake, J. A. Rodriguez and J. F. Weaver, *Accounts Chem. Res.*, 2020, **53**, 1488-1497.
4 C. Zhang, C. Ren, S. Zhang, H. Xue, Y. Zhao, Z. Zhou, J. Chen, Z. Luo, W. Sang, L. Jing, Y. Teng, Q. Qiu, C. Zhang, M. Gong, G. Zhang, T. Shao and L. Xiao, *Energ. Fuel.*, 2021, **35**, 13930-13936.
5 *Energ. Environ. Sci.*, 2019, **12**, 15.
6 H. M. Torres Galvis, J. H. Bitter, T. Davidian, M. Ruitenbeek, A. I. Dugulan and K. P. de Jong, *J. Am. Chem. Soc.*, 2012, **134**, 16207-16215.
7 G. H. Torres, J. H. Bitter, C. B. Khare, M. Ruitenbeek, A. I. Dugulan and K. P. de Jong, *Science*, 2012, **335**, 835-838.
8 P. Tian, Y. Wei, M. Ye and Z. Liu, *ACS Catal.*, 2015, **5**, 1922-1938.
9 Y. Z. X. X. Junwei Xu, 2019.
10 .
11 .
12 .
13 X. Guo, G. Fang, G. Li, H. Ma, H. Fan, L. Yu, C. Ma, X. Wu, D. Deng, M. Wei, D. Tan, R. Si, S. Zhang, J. Li, L. Sun, Z. Tang, X. Pan and X. Bao, *Science*, 2014, **344**, 616-619.
14 P. Xie, T. Pu, A. Nie, S. Hwang, S. C. Purdy, W. Yu, D. Su, J. T. Miller and C. Wang, *ACS Catal.*, 2018, **8**, 4044-4048.
15 A. L. Dipu, S. Ohbuchi, Y. Nishikawa, S. Iguchi, H. Ogihara and I. Yamanaka, *ACS Catal.*, 2019, **10**, 375-379.
16 P. Schwach, X. Pan and X. Bao, *Chem. Rev.*, 2017, **117**, 8497-8520.
17 Z. Liu, E. Huang, I. Orozco, W. Liao, R. M. Palomino, N. Rui, T. Duchoň, S. Nemšák, D. C. Grinter, M. Mahapatra, P. Liu, J. A. Rodriguez and S. D. Senanayake, *Science (American Association for the Advancement of Science)*, 2020, **368**, 513-517.
18 T. Shao, R. Wang, C. Zhang and P. Yan, *High voltage*, 2018, **3**, 14-20.
19 S. Xu, S. Chansai, C. Stere, B. Inceesungvorn, A. Goguet, K. Wangkawong, S. F. R. Taylor, N. Al-Janabi, C. Hardacre, P. A. Martin and X. Fan, *Nature Catalysis*, 2019, **2**, 142-148.
20 .
21 Y. Gao, S. Zhang, H. Sun, R. Wang, X. Tu and T. Shao, *Appl. Energ.*, 2018, **226**, 534-545.
22 .
23 X. X. T. Chao, *J. Energy Chem.*, 2013, **22**, 420-425.
24 J. Kim, J. Jeoung, J. Jeon, J. Kim, Y. S. Mok and K. Ha, *Chem. Eng. J.*, 2019, **377**, 119896.
25 H. Sun, S. Zhang, Y. Gao, B. Huang, C. Zhang and T. Shao, *Plasma Process. Polym.*, 2019, **16**, 1900050.
26 .
27 X. Li, C. Lin, C. Shi, Y. Xu, Y. Wang and A. Zhu, *Journal of Physics D: Applied Physics*, 2008, **41**, 175203.
28 J. Bae, M. Lee, S. Park, M. Jeong, D. Hong, Y. D. Kim, Y. Park and Y. K. Hwang, *Catal. Today*, 2017, **293-294**, 105-112.
29 A. Beloqui Redondo, E. Troussard and J. A. van Bokhoven, *Fuel Process. Technol.*, 2012, **104**, 265-270.
30 I. Julian, H. Ramirez, J. L. Hueso, R. Mallada and J. Santamaria, *Chemical engineering journal (Lausanne, Switzerland : 1996)*, 2019, **377**, 119764.
31 A. H. Khoja, M. Tahir and N. A. S. Amin, *Energ. Convers. Manage.*, 2019, **183**, 529-560.
32 Z. Guo, Y. Yi, L. Wang, J. Yan and H. Guo, *ACS Catal.*, 2018, **8**, 10219-10224.
33 B. Huang, C. Zhang, H. Bai, S. Zhang, K. K. Ostrikov and T. Shao, *Chemical engineering journal (Lausanne, Switzerland : 1996)*, 2020, **396**, 125185.
34 M. Janda, V. Martišovitš, A. Buček, K. Hensel, M. Molnár

and Z. Machala, *Journal of physics. D, Applied physics*, 2017, **50**, 425207.
35 Z. Hu, X. Liu, D. Meng, Y. Guo, Y. Guo and G. Lu, *ACS Catal.*, 2016, **6**, 2265-2279.
36 X. Hu, X. Fu, W. Wang, X. Wang, K. Wu, R. Si, C. Ma, C. Jia and C. Yan, *Applied Catalysis B: Environmental*, 2020, **268**, 118424.
37 W. Yu, W. Wang, S. Li, X. Fu, X. Wang, K. Wu, R. Si, C. Ma, C. Jia and C. Yan, *J. Am. Chem. Soc.*, 2019, **141**, 17548-17557.
38 T. P. Senftle, A. C. T. van Duin and M. J. Janik, *ACS Catal.*, 2017, **7**, 327-332.
39 H. Mai, L. Sun, Y. Zhang, R. Si, W. Feng, H. Zhang, H. Liu and C. Yan, *The Journal of Physical Chemistry B*, 2005, **109**, 24380-24385.
40 .
41 *Fuel*, 1948.
42 .
43 G. J. M. Hagelaar and L. C. Pitchford, *Plasma Sources Sci. T.*, 2005, **14**, 722-733.
44 R. K. Janev and D. Reiter, *Phys. Plasmas*, 2002, **9**, 4071-4081.
45 R. K. Janev and D. Reiter, *Phys. Plasmas*, 2004, **11**, 780-829.
46 J. Hao, P. Schwach, G. Fang, X. Guo, H. Zhang, H. Shen, X. Huang, D. Eggart, X. Pan and X. Bao, *ACS Catal.*, 2019, **9**, 9045-9050.
47 L. Wang, Y. Yi, H. Guo and X. Tu, *ACS Catal.*, 2017, **8**, 90-100.
48 W. Wang, W. Yu, P. Du, H. Xu, Z. Jin, R. Si, C. Ma, S. Shi, C. Jia and C. Yan, *ACS Catal.*, 2017, **7**, 1313-1329.
49 H. A. Calderon, A. Okonkwo, I. Estrada-Guel, V. G. Hadjiev, F. Alvarez-Ramírez, F. C. Robles Hernández and B. C. U. S. Lawrence Berkeley National Lab. LBNL, *Advanced structural and chemical imaging*, 2016, **2**, 1-12.
50 K. Han, W. Yu, L. Xu, Z. Deng, H. Yu and F. Wang, *Fuel (Guildford)*, 2021, **291**, 120182.
51 A. K. Hill and L. Torrente-Murciano, *Applied catalysis. B, Environmental*, 2015, **172-173**, 129-135.
52 Y. A. Kim, K. Fujisawa, H. Muramatsu, T. Hayashi, M. Endo, T. Fujimori, K. Kaneko, M. Terrones, J. Behrends, A. Eckmann, C. Casiraghi, K. S. Novoselov, R. Saito and M. S. Dresselhaus, *ACS Nano*, 2012, **6**, 6293-6300.
53 .
54 S. Hinokuma, H. Fujii, M. Okamoto, K. Ikeue and M. Machida, *Chem. Mater.*, 2010, **22**, 6183-6190.
55 .
56 .
57 .
58 .
59 Z. Xie, B. Yan, S. Kattel, J. H. Lee, S. Yao, Q. Wu, N. Rui, E. Gomez, Z. Liu, W. Xu, L. Zhang, J. G. Chen, U. N. U. S. Brookhaven National Lab. BNL and A. I. U. S. Argonne National Lab. ANL, *Applied catalysis. B, Environmental*, 2018, **236**, 280-293.
60 A. Wang, J. H. Harrhy, S. Meng, P. He, L. Liu and H. Song, *Energ. Convers. Manage.*, 2019, **191**, 93-101.
61 X. Wang, Y. Gao, S. Zhang, H. Sun, J. Li and T. Shao, *Appl. Energ.*, 2019, **243**, 132-144.
62 Y. Yi, X. Wang, A. Jafarzadeh, L. Wang, P. Liu, B. He, J. Yan, R. Zhang, H. Zhang, X. Liu, H. Guo, E. C. Neyts and A. Bogaerts, *ACS Catal.*, 2021, **11**, 1765-1773.
63 Y. Li, D. Yang, J. Qiao, L. Zhang, W. Wang, Z. Zhao, X. Zhou, H. Yuan and W. Wang, *Plasma Sources Sci. T.*, 2020, **29**, 55004.
64 H. Wang, D. Yang, Q. Xu, H. Yuan, X. Zhou and W. Wang, *Journal of physics. D, Applied physics*, 2020.
65 L. Y. Jia, A. Farouha, L. Pinard, S. Hedan, J. D. Comparot, A. Dufour, K. Ben Tayeb, H. Vezin and C. Batiot-Dupeyrat, *Applied Catalysis B: Environmental*, 2017, **219**, 82-91.
66 .

校对报告

当前使用的样式是 [sustainable energy fuels]
当前文档包含的题录共86条
有0条题录存在必填字段内容缺失的问题
66 所有题录的数据正常